Crack growth study of wood and transparent wood-polymer composite laminates by in-situ testing in weak TR-direction

Composites: Part A 173 (2023) 107693

Contents lists available at ScienceDirect

Composites Part A

journal homepage: www.elsevier.com/locate/compositesa

Crack growth study of wood and transparent wood-polymer composite laminates by in-situ testing in weak TR-direction

Nicolò Arcieri [a,b], Bin Chen [a], Lars A. Berglund [a], Marcus Vinícius Tavares da Costa [a,c,*]

[a] Royal Institute of Technology (KTH), Department of Fibre and Polymer Technology, Wallenberg Wood Science Center, SE-100 44 Stockholm, Sweden
[b] Politecnico di Torino, Department of Applied Science and Technology, C.so Duca degli Abruzzi 24, 10129 Turin, Italy
[c] Karlstad University, Department of Engineering and Chemical Sciences, SE-651 88 Karlstad, Sweden

ARTICLE INFO

Keywords:
A. Biocomposites
B. Laminates
C. Fracture
D. Microstructural analysis

ABSTRACT

TW transparent wood/polymer biocomposite laminates are of interest as multifunctional materials with good longitudinal modulus, tensile strength and optical transmittance. The effect of filling the pore space in wood with a polymer matrix on fracture toughness and crack growth is not well understood. Here, we carried out in-situ fracture tests on neat birch wood and laminates made of four layers of delignified birch veneers impregnated with poly(methyl methacrylate) (PMMA) and investigated crack growth in the tangential-radial (TR) fracture system. Fracture toughness K_{Ic} and J_{Ic} at crack initiation were estimated, including FEM analysis. SEM microscopy revealed that cracks primarily propagate along the ray cells, but cell wall peeling and separation between the PMMA and wood phases also take place. A combination of in-situ tests and strain field measured by digital image correlation (DIC) showed twice as long fracture process zone of TW laminates compared with neat birch.

1. Introduction

Wood has been used as a structural material for millennia [1]. However, steel and concrete have substituted wood in many load-bearing applications [2]. Nowadays, the interest in wood and wood-based materials is again growing due to the positive environmental effects from materials with renewable resource origin. A promising class of wood-based materials for structural applications is wood-polymer biocomposites prepared by filling the pore space with polymer, due to their mechanical performance and low density [3]. Wood-polymer biocomposites are used for boat decking, sports equipment, flooring, and even as engineering materials in small wind turbine blades and propeller blades [4], where the polymer phase improves elastic stiffness and strength accompanied by an improved surface finish, hardness, dimensional and moisture stability, and biodeterioration resistance [5]. A new version of such composites is transparent wood (TW) biocomposites which have similar characteristics with the added functionality of optical transmittance. It is significant that different species of neat wood have different porosity and therefore different density, although the wood cell wall has similar density for all wood species (≈1500 kg/m^3). The mechanical properties of wood therefore scale with relative density (sample density divided by wood cell wall density) which is the volume fraction of solid cell wall.

TW biocomposites are produced by impregnating a wood template without chromophores with a refractive index-matching polymer [6,7]. During the synthesis, delignification or bleaching is essential to remove chromophores, while increased nanoscale porosity can help the polymer to enter inside the wood cell wall and lumen [3,8]. The matching of the refractive indices of the two constituents yields a biocomposite with high optical transmittance, making it a potential alternative in the building sector e.g., in assemblies of construction panels in buildings to convert the sunlight into evenly diffusive indoor light [9–11]. In addition, dimensional moisture stability is improved, which makes such composites more attractive in construction [12]. The optical transmittance of TW biocomposites can reach up to 90 % for 3 mm thick slabs [7], which is not far from neat poly (methyl methacrylate) (PMMA) [13]. The combined structural-optical properties of TW biocomposites have generated interest in TW laminates, where mechanical properties can be fine-tuned by varying the orientation of veneer layers [3,14]. The lamination strategy also overcomes limitations in thickness from the delignification process [11]. Increasing wood substrate thickness makes uniform chemical delignification and complete monomer impregnation more difficult. Typically, the lamination strategy uses thin wood veneers (a few millimetres) as starting material [8,11]. Effects of the polymer

* Corresponding author at: Karlstad University, Department of Engineering and Chemical Sciences, SE-651 88 Karlstad, Sweden.
E-mail address: marcus.tavares@kau.se (M.V. Tavares da Costa).

https://doi.org/10.1016/j.compositesa.2023.107693
Received 4 April 2023; Received in revised form 8 July 2023; Accepted 10 July 2023
Available online 11 July 2023

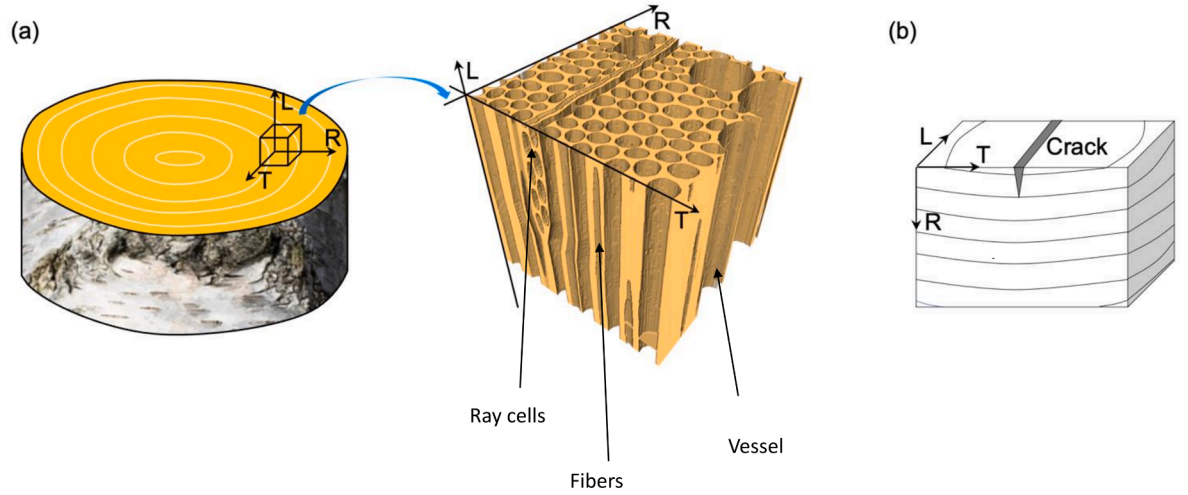

Fig. 1. Representation of internal wood structure. a) Schematic sketch showing axes orientation in the coordinate system of the trunk of a tree to the wood microstructure. L longitudinal, R radial, T tangential b) TR fracture system.

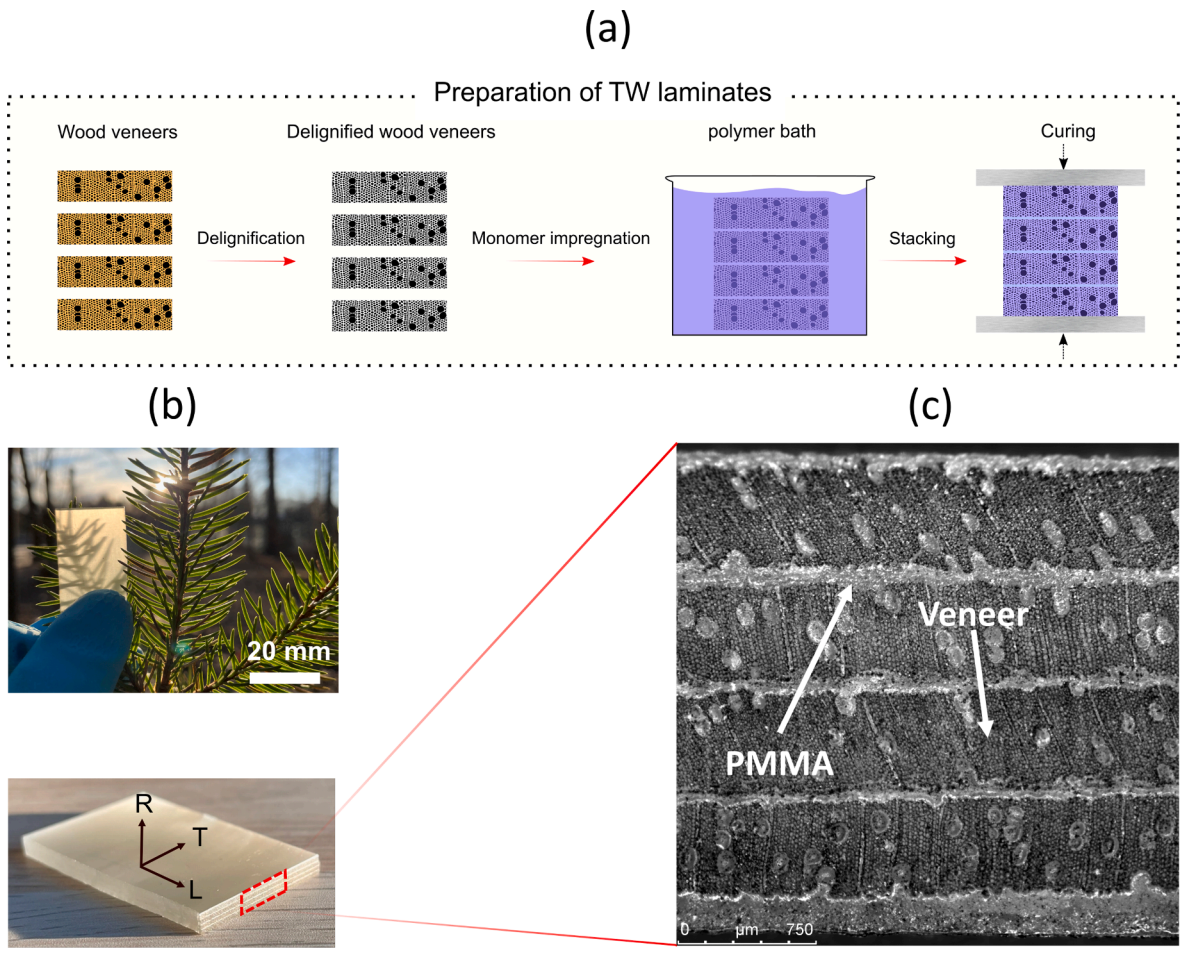

Fig. 2. TW laminates. (a) Process of sample preparation of the TW laminate, (b) photograph of the TW laminate and its wood material axis, (c) cross section of the transparent wood laminate where the fibre direction is perpendicular to the plane of the image. Interfibre adhesive PMMA bond lines between veneer layers are oriented horizontally.

matrix on fracture toughness as compared with neat wood are not well understood.

Although the mechanical performance of wood is significantly enhanced with infiltrated polymer phase, the main efforts to study TW composites have been devoted to characterizing and tailoring optical, thermal and other functional properties [3,6,8,9,15–18]. A few studies have investigated the mechanical properties [7,14,19–22], where moduli and strengths are reported. The studies often sought to find global mechanical properties to compare to classical engineering composites. Only limited efforts have been published on fracture mechanics

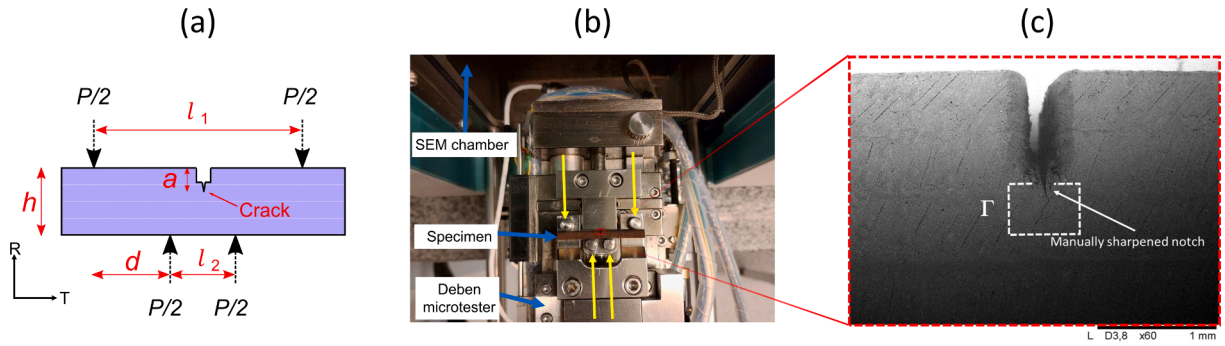

Fig. 3. Setup for in situ single-edge-notched four-point bending test. (a) Final notch shape in TW laminates with dimensions. (b) Specimen placed in Deben microtester before being inserted in the SEM chamber. (c) SEM image of the notch.

Table 1
Mechanical properties of transparent wood and its constituents.

Properties	Native birch	PMMA [14,41]	TW laminate
E_T (GPa)	0.5 ± 0.1	2.4	3.3 ± 0.0
MOR_T (MPa)	11.6 ± 0.8	117.9	17.2 ± 2
V_f(%)	41	–	23
ν_{TR}	0.38 [33]	0.35	0.36

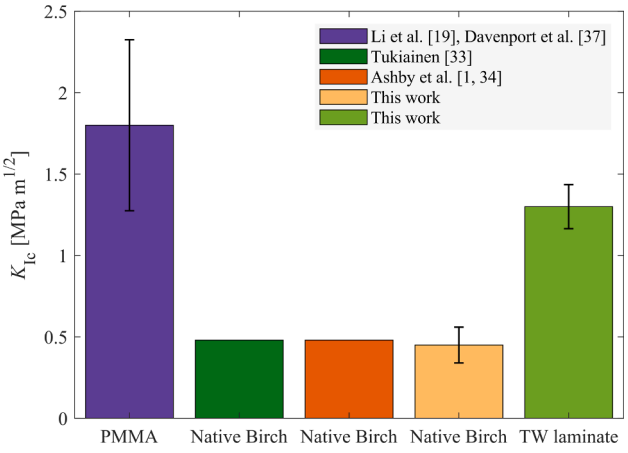

Fig. 4. Bar chart of fracture toughness data for different materials.

properties [19,21,22]. To clarify the fracture planes in wood and wood-polymer composites, Fig. 1 illustrates the tangential-radial (TR) system: (a) the arrangement of the principal axes in wood from the trunk to the microstructure and (b) a definition of TR crack propagation (opening tension in tangential T direction and radial R direction of crack growth), i.e., the first index represents the direction of the opening tension, and the second index represents the crack growth direction.

In a recent TW study by Jungstedt et al. [22], a FEM updating protocol was developed to characterize fracture mechanics properties by optimizing displacement fields obtained from digital image correlation (DIC) measurements with finite element (FE) simulations. Jungstedt et al. [22] studied birch/PMMA for crack growth in the weak TL direction and used a cohesive zone model to describe the behavior of a fracture process zone (FPZ); energy dissipation mechanisms were discussed, as in related investigations [23,24]. Crack growth and toughness of wood can be described by fracture mechanics to correlate global behavior with local crack growth and damage [25,26]. For TW biocomposites, balsa/PMMA of low wood content have been investigated to determine fracture toughness in tough (LT) and weak (TL) systems [19]. In Ref. [21], wood laminates were investigated, where the initiation value for fracture toughness K_{Ic} in LT system (crack growing in toughest direction perpendicular to fibre direction) was around 3 MPa m$^{1/2}$, similar as data in Ref. [19].

Microscale fracture mechanisms of TW biocomposites have not been sufficiently investigated, and may contribute to the development of wood-polymer composites of improved toughness properties. Observations of polymer matrix effects and how crack growth interacts with wood cells, vessels and rays (filled with the polymer) may help to tailor volume fraction of wood reinforcement, wood-polymer interface properties and polymer matrix properties.

The purpose of this study is primarily to investigate polymer matrix effects on damage mechanisms in the TW laminate microstructure for crack growth in the weak TR system by in-situ SEM microscopy carried out during fracture mechanics testing. Failure in structural wood sys-

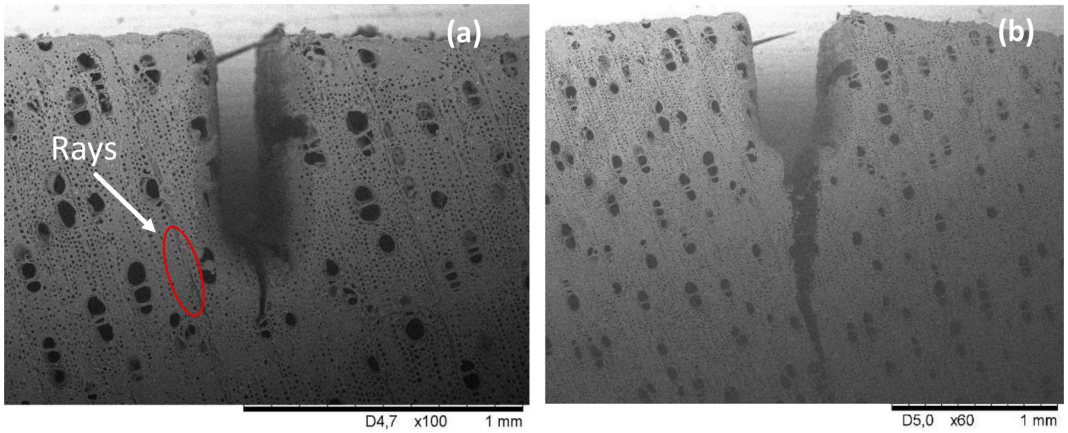

Fig. 5. Native Birch. Micrographs (a) before and (b) after crack propagation.

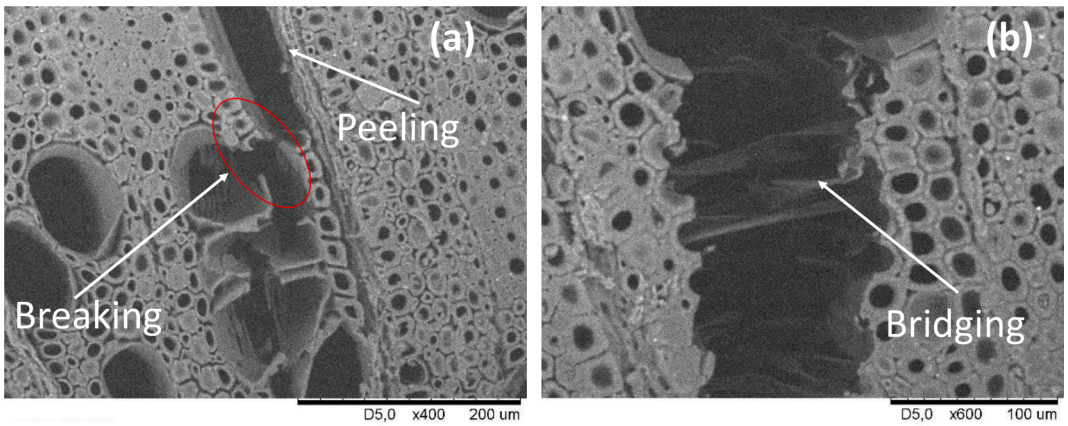

Fig. 6. Higher magnification micrographs of the fracture in native birch. (a) cell wall separation and cell wall fracture (b) cross fibre bridging.

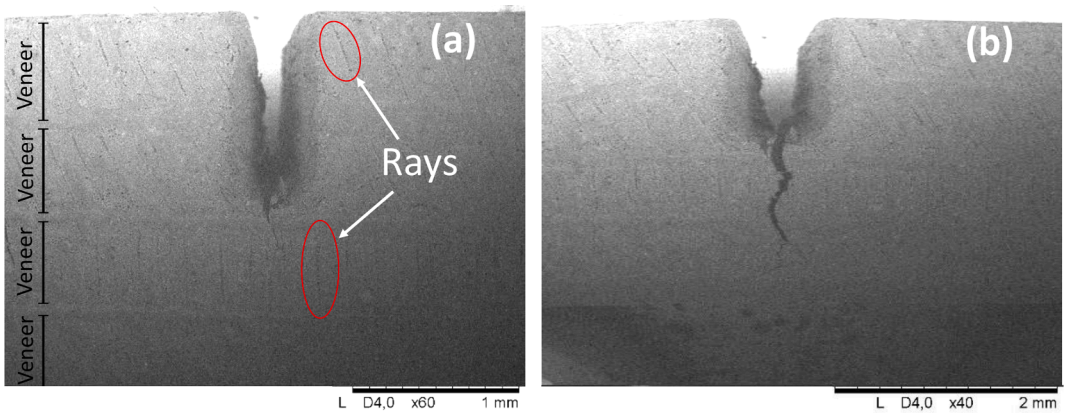

Fig. 7. TW laminate. Micrographs (a) before and (b) after crack propagation.

tems (e.g., at joints) is often initiated by cracks growing in weak directions between fibres [26]. For the present work, the choice of the system is helpful since many microstructural wood features, such as vessels, fibres and rays can be observed during crack propagation. The samples were prepared by stacking layers of delignified birch veneers impregnated with PMMA with fibre orientation $[0]_4$. As a secondary aim, we seek to determine fracture toughness at crack growth initiation from the tests using the J-integral approach in three different ways: DIC strain-field measurements, load–deflection measurements and FE simulations. In particular, the DIC strain-field gradients measured from cross-sectional micrographs at crack onset were used to estimate the fracture energy J_{Ic} in the laminates. These results were compared with results from FE modelling and load–displacement approaches. The size of the FPZ was estimated from strain fields for both the TW laminate and birch.

2. Materials and methods

2.1. Preparation of TW laminates

Four-layer TW laminates $[0]_4$ were prepared based on veneer; Birch (*Betula Pendula*) veneers of 0.5 mm thickness were used. They were purchased from Calexico Wood AB (Sweden). All veneers had the fibre direction parallel to the surface. Four veneers were cut into size 100 × 100 mm^2. The process of TW preparation is shown in Fig. 2(a). The first stage of preparation was the delignification, which was performed in accordance with the $NaClO_2$ method [3,9,14,27]. Delignification involved soaking the veneers in an acetate buffer solution (pH = 4.6) containing 1.25 wt% $NaClO_2$. The veneers were left in solution at 75 °C until they turned whitish. Then, the delignified veneers were thoroughly washed under vacuum with deionized water three times. This step was followed by dehydration, using ethanol and then acetone (three times, under vacuum). The next step was polymer infiltration with PMMA. Liquid methyl methacrylate (Aldrich) was pre-polymerized at 75 °C. After 10–15 min, polymerization was interrupted by placing the flask in an ice bath. Then, the delignified veneers were immersed in the pre-polymer bath for vacuum infiltration (overnight). After this step, they were tightly packed between two glass plates, making sure that all veneers had the fibres oriented in the same direction. Finally, the samples were wrapped in aluminium foils and cured at 70 °C for 4 h to promote polymerization. As a result, a 3 mm thick transparent wood biocomposite laminate was produced (c.f. Fig. 2(b)). The final material thickness was the sum of that of the veneers and that of the PMMA layers.

The volume fraction of the wood cell wall of the laminate and native birch was evaluated. For the TW laminate, the volume fraction was obtained as follows [28]:

$$V_{TW} = \frac{W_{cell}\rho_c}{\rho_{cell}} \quad (1)$$

where W_{cell} defines the cellulose weight fraction (0.28), ρ_c is the density of the composite (1259 kg/m^3), and ρ_{cell} is the density of the cellulose (1500 kg/m^3) [28]. The cellulose weight fraction W_{cell} was obtained by dividing the weight of the delignified veneers by the total weight while ρ_c was calculated by dividing the weight of the composite by its volume.

The volume fraction in neat wood is equal to its relative density, which was calculated as [14]:

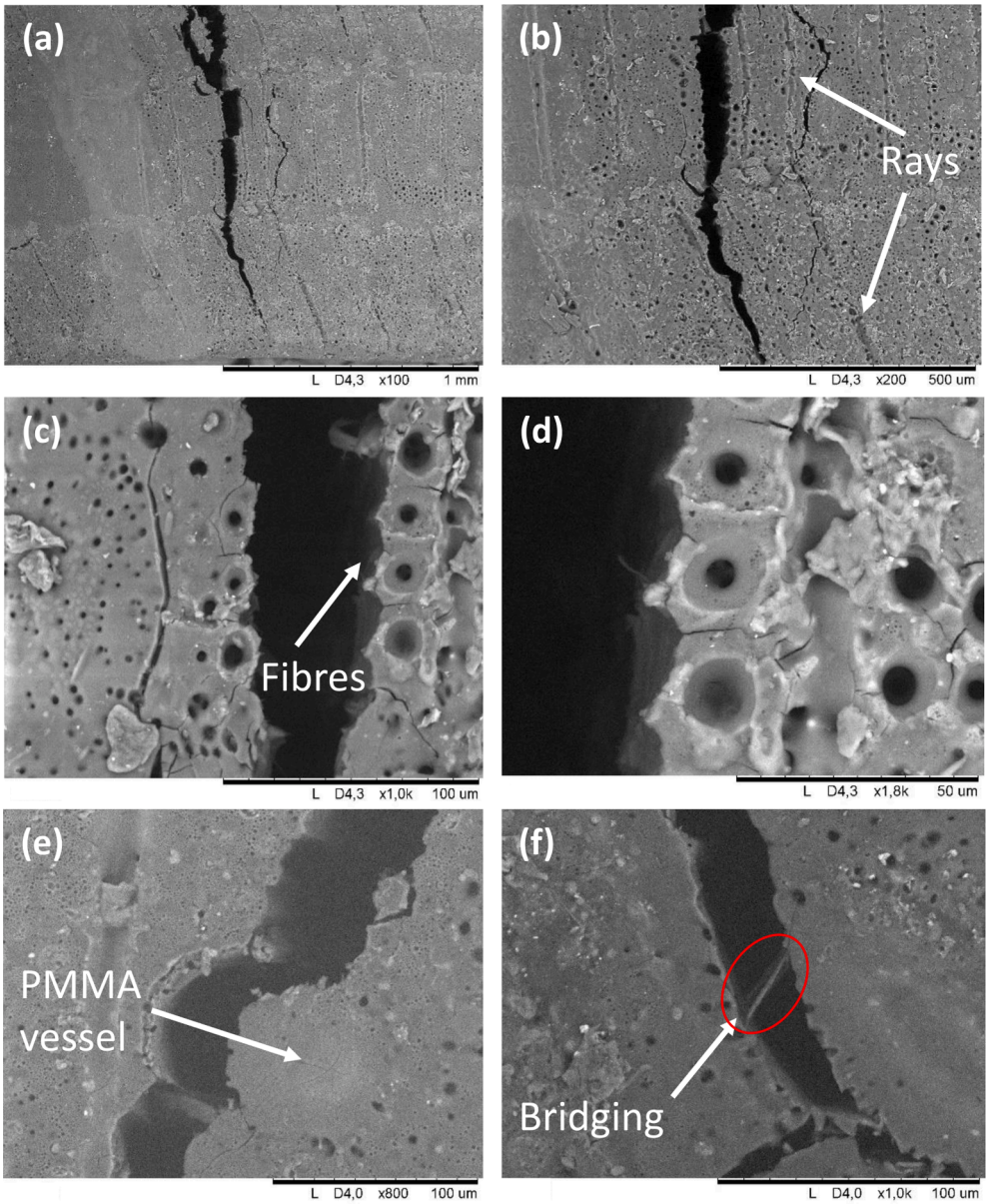

Fig. 8. TW laminate with higher magnification. (a)–(b) crack propagation, (c)–(d) cell wall peeling, (e) vessel cell wall-polymer debonding, and (f) fibre bridging.

$$V_{NW} = \frac{\rho_{Birch}}{\rho_{cell}} \tag{2}$$

where ρ_{Birch} is the density of native birch (612 kg/m^3). It is assumed that the density of the cell wall (ρ_{cell}) was equal to that of cellulose.

Before mechanical tests, the cross-section of the specimens was examined by an optical microscope (Leica M205 FA) connected to a digital camera (Hamamatsu C11440) as shown in Fig. 2(c).

2.2. Experimental setup for the four-point bending tests

For the four-point bending test, three specimens were cut to the size of 70 × 5 × 3 mm^3 for native Birch (NW) and transparent wood (TW) with a portable scroll saw (Dremel, Moto-Saw MS20-15). NW samples were cut from a 3 mm thick Birch board (Calexico Wood AB). All specimens were produced by ensuring that the fibre direction was parallel to the short side of the sample.

During the experiment, the tangential elastic modulus, E_T, as well as the tangential modulus of rupture were studied. An Instron 5566 Universal Testing Machine with a load cell of 500 N was employed to perform the four-point bending test. The experimental setup was carefully chosen based on considerations of beam theory validity and relationship to the in-situ test [29]. The support span was 60 mm and the load span 14 mm. The testing machine was set in displacement control mode with a speed of 0.1 mm/min. The equipment was in an environment-controlled room (22 °C and relative humidity of 50 %). The tangential elastic modulus was obtained using the following equation [29]:

$$E_T = \frac{d^2[3l_1 - 4d]}{bh^3}\frac{dP}{dw} \tag{3}$$

where d is the distance between the support point and the closest loading point, l_1 is the support span, b is the specimen width, and h is its thickness. The dimensions can be conferred in Fig. 3(a) neglecting the crack. The slope $\frac{dP}{dw}$ is calculated from the initial part of the load–deflection curves. The range for calculation was set between 10 % and 50 % of the maximum load, thus considering these values as the lower and upper limits of the elastic part, respectively. In addition, the tangential modulus of rupture (MOR) was calculated using the formula

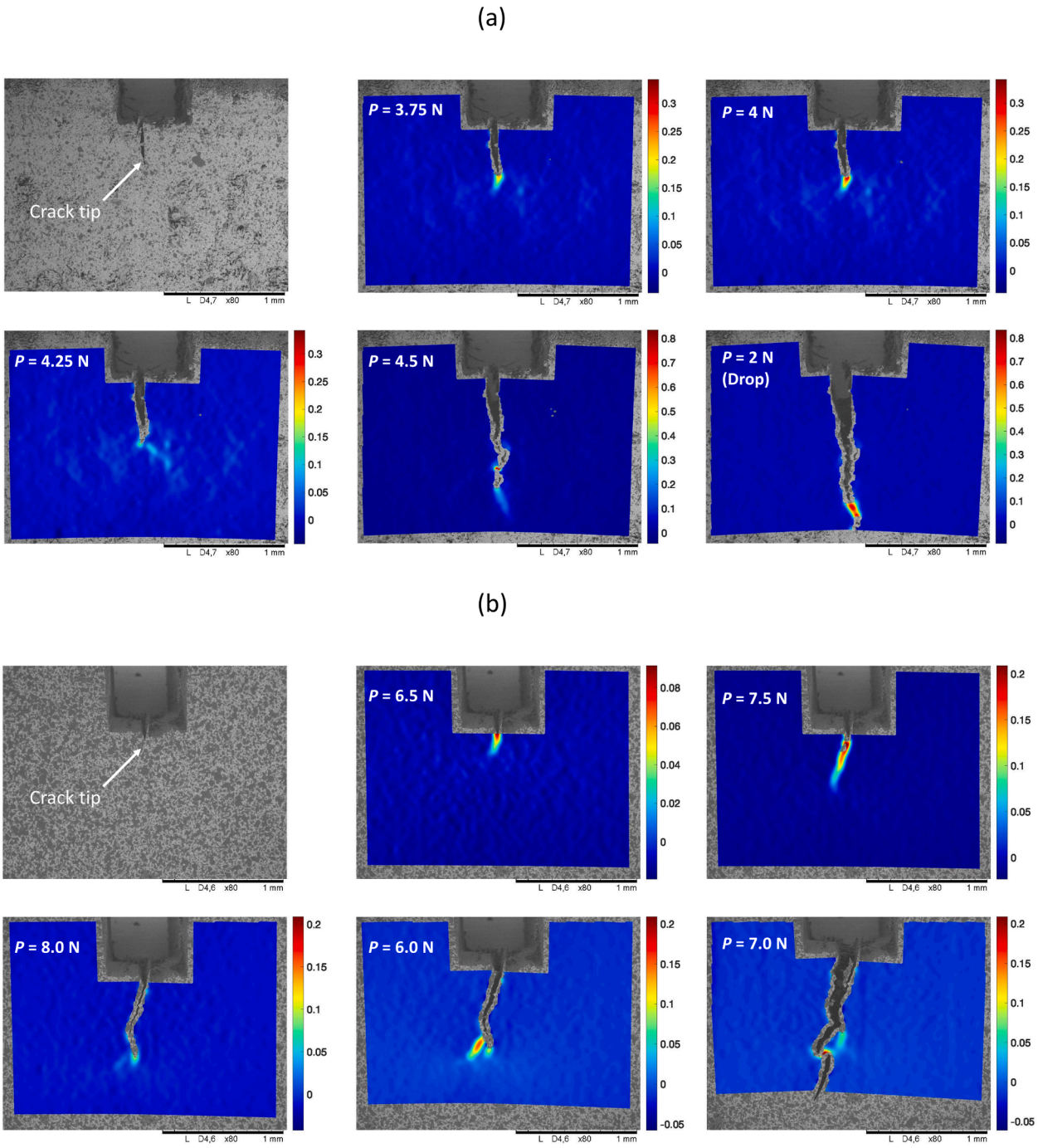

Fig. 9. Strain field ε_T: sequential images during the crack growth in (a) a native Birch sample and (b) a TW laminate. (unit: strain).

[30]:

$$MOR = \frac{3P_c(l_1 - l_2)}{2bh^2} \tag{4}$$

where P_c is the maximum load and l_2 is the load span.

2.3. Experimental setup for in situ single-edge-notched four-point bending test

2.3.1. Fracture toughness of TW laminates

The in situ single-edge-notched four-point bending specimens were produced by laser cutting (Redsail CM1490) to have more control and precision in the geometry (see Fig. 3). Here, three specimens of the size of $30 \times 3 \times 3$ mm^3 with an initial notch of 1 mm were prepared for each material. Then, the crack was manually sharpened by a razor blade as shown in Fig. 3(c). The sharpness was verified on both sides of the samples with the optical microscope before the fracture tests.

A Deben Microtest 200 N was used to perform the in-situ tests. The instrument was equipped with a 50 N load cell and housed inside a tabletop scanning electron microscope (SEM, Hitachi TM-1000), as shown in Fig. 3(b). The tabletop SEM was operating at an accelerating voltage of 15 kV. The micrograph images were acquired throughout the tests before and after crack propagation. The in-situ tests were carried out at a deflection rate of 0.1 mm/min, with a loading span of 5.5 mm and a support span of 23 mm. ImageJ software was employed to measure the initial crack length from the micrographs.

Here, the fracture toughness was estimated from the load–deflection

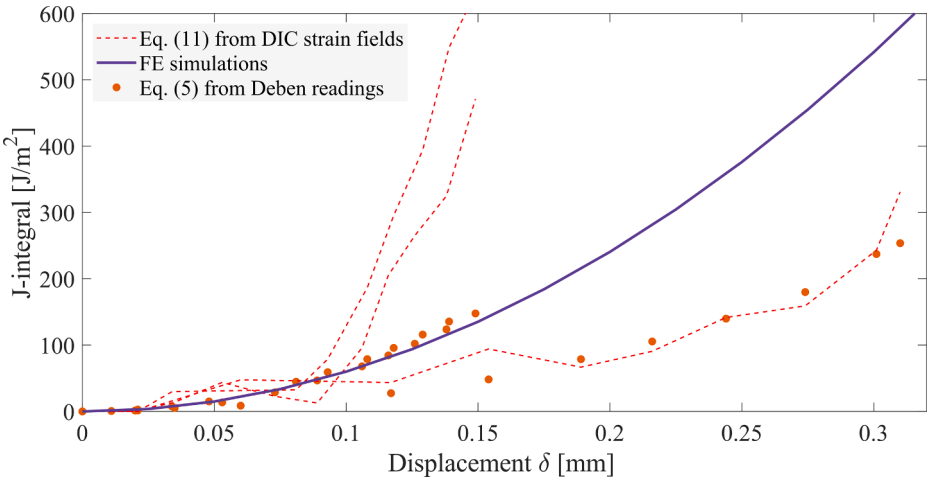

Fig. 10. Computed J-integral for three TW specimens by different techniques from the stepwise tests: Strain fields (with Eq. (8)), force–displacement from Deben microtester and finite element simulations.

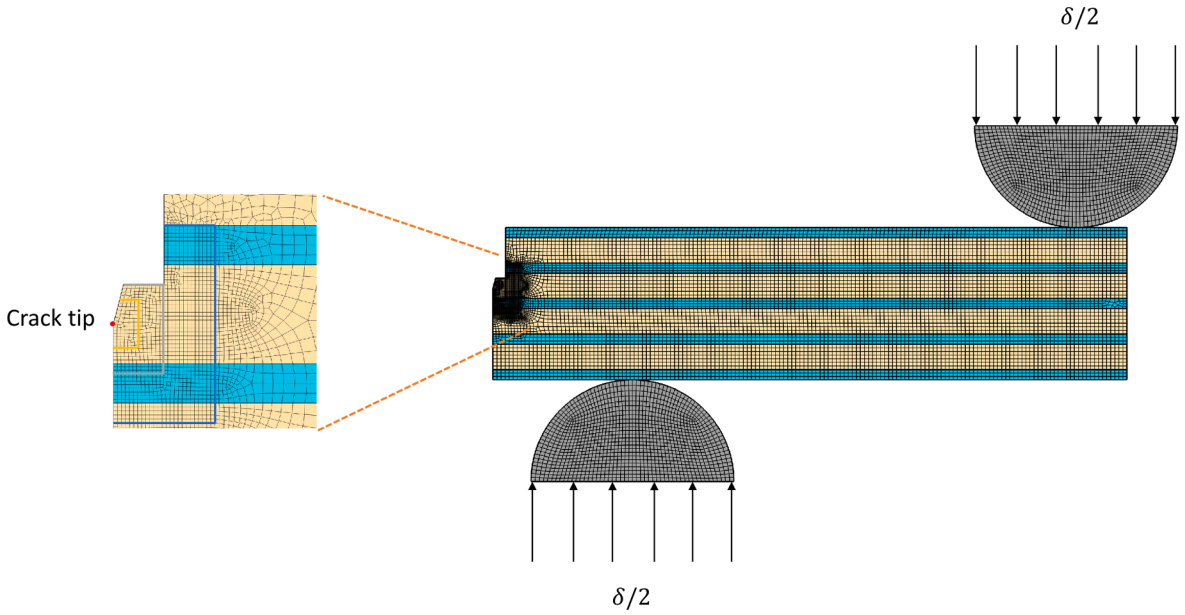

Fig. A1. Finite element model of half of the tested TW laminates. Three contours were evaluated around the crack tip as shown on the left: 0.25, 0.5, and 1 mm from the crack tip.

readings recorded by the microtest up to the crack onset (c.f. Fig. A.2 (a)). The J-integral for critical load was calculated as [21,31]

$$J_{Ic} = \frac{2U(P_c)}{(h-a)b} \tag{5}$$

where $U(P_c)$ is the area under the curve load vs loading-line deflection evaluated at the critical load, h is the sample thickness, a is the crack length and b is the width of the specimen. Then, J_{Ic} was converted into the equivalent critical stress intensity factor as follows [21,32]:

$$K_{Ic} = \left(J_{Ic} E_T \left(1 - {\nu_{TR}}^2\right)\right)^{1/2} \tag{6}$$

where E_T is Young's modulus in the tangential direction measured in 2.2 and ν_{TR} is the Poisson's ratio for the TR system. Due to the lack of data in the literature for the Poisson's ratios of TW laminates, $\nu_{TR} \approx 0.36$ for the laminate was approximated as a value between a lower bound from PMMA $\nu_{PMMA} = 0.35$ and an upper bound from TW slabs in LT wood plane $\nu_{LT} = 0.38$ [14]. For native birch, ν_{TR} is 0.38 [33].

As an alternative, the critical stress intensity factor can also be roughly predicted by the following scaling law equation [1,34]:

$$K_{Ic} = 1.8\left(\frac{\rho_{Birch}}{\rho_{cell}}\right)^{3/2} \tag{7}$$

developed empirically by Ashby et al. [34]. ρ_{Birch} is the density of porous birch wood and ρ_{cell} is the density of the wood cell wall (≈1500 kg/m^3). This model provides "rule of thumb" estimates for the fracture toughness of neat wood when a crack propagates in the TR-direction [1,34].

2.3.2. Strain field measurements

Three samples for each material were prepared in the same way as described in the previous section. Here, the specimens were studied by means of in-situ experiments coupled with the DIC technique, in order to study the strain field of the materials and the growth of the micro defects. A thin layer of white base ink was sprayed, followed by black ink speckles to generate a high-contrast random speckle pattern for the DIC analysis. Before crack propagation, the test was stopped roughly every

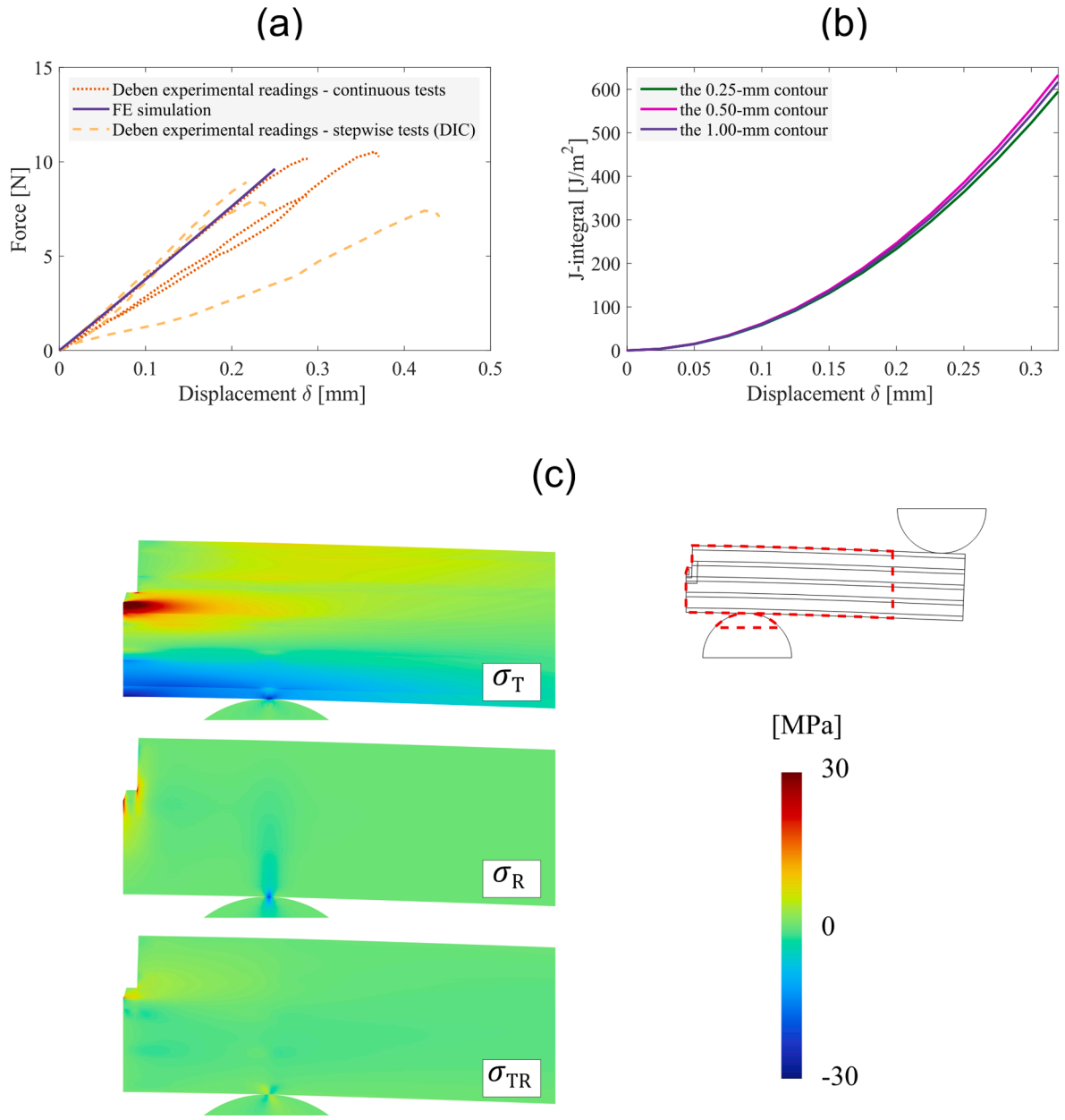

Fig. A2. (a) Comparison of force–displacement curves from experimental tests on three specimens and simulations and (b) computed J-integral from the three stress field contours. (c) Below the complex stress fields at the crack tip at displacement of 0.3 mm are shown in the TR plane.

0.25 N to take an image of the specimen. After the crack started to grow, images were acquired in accordance with changes in the behaviour of the crack with a magnification of 80 × . The latter images were only acquired for the purpose of strain field measurements. For each sample tested, at least of 13 SEM images (1280 × 1100 pixels) was recorded, where the scale was 1 pixel ≈ 1.83 μm. The software VIC-2D 6 (Correlated Solutions, Inc.) was used to retrieve the strain distribution on the sample surface. The displacement maps were measured with a subset size of 35 × 35 pixels and a constant step size of 5 pixels. The strain fields were then calculated using a filter window size of 7 × 7 points.

As a source of comparison, we also calculated the fracture energy here. From the retrieved strain maps, the J-integral can be theoretically calculated using the energy line integral following the definition given by Rice, 1968[35]:

$$J_{\mathrm{I}} = \int_{\Gamma} W d\mathrm{T} - \mathbf{F}\frac{\partial \mathbf{u}}{\partial \mathrm{R}} ds \tag{8}$$

where Γ is a selected counter clockwise path around the crack tip and ds is the length increment along the integration path Γ. The vectors $\mathbf{F} = \sigma_{ij}\mathbf{n}$ is the traction vector and $\mathbf{u} = (u_{\mathrm{T}}, u_{\mathrm{R}})$ is the displacement vector. The strain energy density W is defined as

$$W = \int_0^{\varepsilon_{ij}} \sigma_{ij} d\varepsilon_{ij} = \frac{1}{2}[\sigma_{\mathrm{T}}\varepsilon_{\mathrm{T}} + \sigma_{\mathrm{R}}\varepsilon_{\mathrm{R}} + 2\sigma_{\mathrm{TR}}\varepsilon_{\mathrm{TR}}] \tag{9}$$

where σ_{R}, σ_{T}, σ_{TR} and ε_{R}, ε_{T}, $\varepsilon_{\mathrm{TR}}$ are the radial, tangential and shear stresses and strains, respectively. The stress components are calculated by Hooke's law based on orthotropic material as

$$\begin{bmatrix} \sigma_{\mathrm{T}} \\ \sigma_{\mathrm{R}} \\ \sigma_{\mathrm{TR}} \end{bmatrix} = \frac{1}{1-\nu_{\mathrm{TR}}\nu_{\mathrm{RT}}} \begin{bmatrix} E_{\mathrm{T}} & \nu_{\mathrm{RT}}E_{\mathrm{T}} & 0 \\ \nu_{\mathrm{TR}}E_{\mathrm{R}} & E_{\mathrm{R}} & 0 \\ 0 & 0 & G_{\mathrm{TR}}(1-\nu_{\mathrm{TR}}\nu_{\mathrm{RT}}) \end{bmatrix} \begin{bmatrix} \varepsilon_{\mathrm{T}} \\ \varepsilon_{\mathrm{R}} \\ 2\varepsilon_{\mathrm{TR}} \end{bmatrix} \tag{10}$$

where the radial, tangential and shear modulus used in this work are 4.0, 3.3, 0.1 GPa for TW laminate, respectively. The strain components

are measured by DIC. Rewriting the J-integral for TR fracture system leads to [36]

$$J_{\mathrm{I}} = \int_{\Gamma} W d\mathrm{T} - \int_{\Gamma}\left(\sigma_{\mathrm{R}}\frac{\partial u_{\mathrm{R}}}{\partial \mathrm{R}} + \sigma_{\mathrm{RT}}\frac{\partial u_{\mathrm{T}}}{\partial \mathrm{R}}\right)d\mathrm{T} + \int_{\Gamma}\left(\sigma_{\mathrm{RT}}\frac{\partial u_{\mathrm{R}}}{\partial \mathrm{R}} + \sigma_{\mathrm{T}}\frac{\partial u_{\mathrm{T}}}{\partial \mathrm{R}}\right)d\mathrm{R} \qquad (11)$$

The rectangular path Γ (see the white dashed line in Fig. 3(c)) around the sharp notch with dimension of around 0.5 × 0.5 mm^2. The displacement gradients $\frac{\partial u_{\mathrm{T}}}{\partial \mathrm{R}}$ and $\frac{\partial u_{\mathrm{R}}}{\partial \mathrm{R}}$ along radial directions are calculated from the displacement field measurements. Note that Eq. (11) was calculated only up to the crack onset as well.

For more detailed information, the readers are referred to Ref. [36].

3. Results and discussion

3.1. Mechanical properties along the tangential direction

The results, shown in Table 1, were obtained from the four-point bending test, wood volume fraction along with the estimated Poisson's ratio. In addition, literature data for PMMA are reported.

The TW laminate is stiffer than both PMMA and neat wood. This increase is due to the suppression of the cell wall bending deformation mechanism by PMMA filling the cell lumen pore space [14]. The tangential modulus of rupture (strength) of the TW laminate in bending is about 50 % higher compared to neat birch (17.2 MPa versus 11.6 MPa). However, TW is still brittle in tangential bending and failure is initiated by defect formation, e.g., wood cell wall-polymer interface debonding.

3.2. Fracture toughness

Fig. 4 shows experimental data for fracture toughness K_{Ic} in the weak tangential TR fracture system of native birch wood and the TW laminate in the present study. Ashby's empirical estimate and literature data for birch [1,33,34] and PMMA [19,37] are also presented. For native birch, NW, the present figures of fracture toughness are in general agreement with values in the literature. In addition, the experimental values of ≈ 0.5 MPa $m^{1/2}$ was close to the estimate based on Eq. (7) (≈ 0.47 MPa $m^{1/2}$) and the value reported in the literature of ≈ 0.5 MPa $m^{1/2}$ [33]. The K_{Ic} of the TW laminate is substantially higher (≈1.3 MPa $m^{1/2}$) than for native birch, approaching the mean value of pure PMMA. As a comparison, although it is not in the same wood fracture plane, Jungstedt et al. [22] reported K_{Ic} = 0.3 MPa $m^{1/2}$ for a single TW lamella in the weak TL fracture system; the higher K_{Ic} obtained here is likely to be a result of differences in ray cell orientation from laminate structure, which will be discussed in the next section. The difference in ray cell orientation eventually promotes a more tortuous crack path for a laminate where slight differences in orientation between layers are inevitable, see Fig. 2(c).

3.3. Crack growth mechanisms

The crack propagation was examined in real-time via in-situ testing in SEM to infer fracture mechanisms. Fig. 5(a)–(c) show the NW specimen before and after testing. Larger vessel cells with diameters at the 100 μm scale are apparent as dark regions, whereas fibre cells have diameters at the scale of 10 μm (apparent as very small dots). Note that the radial ray cell direction is slightly off-axis compared with the initial pre-crack. As can be seen in the SEM images, the crack growth was preferably along the ray cells, in the radial direction as previously suggested for TR cracks [34].

During crack growth in NW, other mechanisms were also observed, as illustrated in the higher magnification images in Fig. 6(a) and (b). The crack mainly propagated in the interfibre region by fibre cell wall peeling (see Fig. 6(a)), although cell wall fractures of the large vessel cells also played an important role. In native wood, the cell wall peeling often occurs in the middle lamella [26]. Cross-over fibre bridging was also observed, see Fig. 6(b). This phenomenon is an energy-dissipation mechanism that is usually not dominant for the TR system [33,34].

In the TW laminate, the crack propagates along the ray cells, similarly to native wood, as shown in Fig. 7(a)–(b). Note the veneer layers oriented horizontally, with adhesive bond-lines in-between. One bond-line is near the tip of the pre-crack, while another one is horizontally in the middle of the pre-crack. The initial pre-crack has an orientation slightly off-axis to radial ray cell direction but deviates along the ray cell radial direction during growth, see Fig. 7(b). The wood substrate morphology strongly influences crack growth also in TW biocomposites.

This observation becomes more evident looking at Fig. 8(a) and (b), where the sample surface is shown at higher magnification. Here, the crack deviated slightly in the vicinity of the bond-line to follow different ray orientations in the two veneer layers. During crack propagation, no delamination was detected between the layers. As in neat birch, cell wall separation was observed (see Fig. 8(c) and (d)). Here, the site of cell wall peeling is again most likely the middle lamella in-between two fibres. This region is lignin-rich in native wood but may contain PMMA [28]. Debonding is also apparent in Fig. 8(e), where the crack propagates at the interface between the inner cell wall of a vessel and the PMMA-rich central region of the cell. Fig. 8(f) shows cross-over fibre bridging for TW, but much less pronounced compared to NW. Another interesting phenomenon was the development of small-scale microcracking damage associated with the main crack (Fig. 8(c)). Finally, the small surface pores observed are artefacts formed during laser cutting of the cross-sections. They did not influence mechanical properties.

3.4. Strain field data

The DIC method [38,39] can be used to follow the development of the strain field in the in-situ microscopy sample. This method allowed to track the strain fields ε_T in a tortuous crack path in NW and TW laminate samples as shown in Fig. 9. The fracture mechanisms of transparent wood and native wood were previously investigated in the TL plane by Jungstedt et al. [20]. For the TR fracture system [33], the elastic energy appears to dominate crack initiation and the crack then propagates unstably (brittle fracture). The FPZ size can be estimate from a frame just before crack growth. Here, a comparison can be made from the strain field ε_T for native birch and a TW laminate just before the start of crack growth; the fields are at forces of ≈4.0 N for NW and at 7.5 N for TW laminate. In Fig. 9, the red region around the crack tip suggests the development of FPZ as it is related to a high strain concentration [20].

In native birch, the presence of the FPZ is related to fibre bridging and microcracks, which are energy dissipation mechanisms in wood and play a major role in increasing the toughness of the material [23,24,40]. However, the limited extension of the FPZ (0.173 mm) means that these toughening phenomena only occur in a small material volume around the crack tip. A similar extension of the FPZ was observed for the entire set of neat wood specimens. These images suggest linear elastic fracture mechanics may describe TR crack growth in wood and be valid for material property data for engineering design [33]. For materials design purposes, one may still benefit from more advanced analyses. Moreover, away from the crack, the strain field was not homogenous. Indeed, wood has a heterogeneous structure with defects and non-uniform anatomy features, in addition to anisotropic strain distribution.

In the TW laminate, the fracture process zone appears to extend over greater material length than in native birch. In this case, the FPZ length was 0.450 mm. Again, the main energy-dissipation phenomena are fibre bridging and microcracking. Unlike native wood, the strain distribution was more uniform away from the crack.

The measured strain field gradients can be used in the calculation of the fracture energy by evaluating Eq. (8) based on strain field DIC data in Fig. 10. The values at initiation of crack propagation from TW specimens show significant scatter among the three samples. The reason is the combined brittle behavior and heterogeneous microstructure. The

alternative analysis is using finite element (FE) simulations (see in the appendix A) and Eq. (5) from Deben data. The procedure differs in that the material is described as orthotropic (appendix A), and the specific geometry of the specimen is included in the numerical FE analysis. Experimental data for critical force is used as crack initiation criterion and the strain field calculated by FEM is used rather than DIC data. The J-integral based on DIC data follows the experimental trends well, but it is strongly influenced by heterogeneities in the microstructure of individual samples. They include non-straight initial cracks, which immediate deflect to the radial ray orientation direction, micro-cracks between the cells and/or vessel walls. The sample with the highest toughness values show crack initiation simultaneously at the crack tip and at other nearby locations (see in the supplemental materials). One may note that the crack in Fig. 9 is less sharp than desired, but this is related to experimental difficulties. The main goal to characterize crack growth micro-mechanisms could still be met.

4. Conclusion

The tangential elastic modulus E_T was strongly improved to 3.3 ± 0.0 GPa by the polymer matrix for the D-birch/PMMA transparent wood laminate with onlyE_T = 0.5 ± 0.1 GPa for native birch while their tangential moduli of rupture (strength) in four-point bending were 17 MPa and 12 MPa, respectively. In-situ single-edge-notched four-point bending experiments made it possible to follow crack initiation and growth in the TR system in real-time (tangential tensile stress, radial direction crack growth). The propagation always occurred along the ray cells and cell wall separation and debonding at PMMA /wood interfaces was observed. Cross-over fibre bridging was observed for both neat birch and transparent D-birch/PMMA, although crack growth was unstable. The fracture toughness K_{Ic} from peak load in the transparent wood laminate was improved by the polymer matrix to 1.3 MPa $m^{1/2}$ while native birch showed a fracture toughness of 0.5 MPa $m^{1/2}$. Combination of in-situ tests and DIC strain field analysis allowed the study of a long and narrow FPZ fracture process zone. The FPZ length was 0.45 mm for transparent wood laminate and 0.17 mm for neat birch. DIC strain field gradients from microscopy images at peak load and isotropic material assumption can be used to directly calculate the fracture energy J_{Ic} at crack initiation with good accuracy. These J_{Ic} values were relatively close to J_{Ic} based on experimental peak load and FE simulation predictions of strain field in an orthotropic material. The measured strain field of native birch showed significant local inhomogeneities in contrast with transparent wood, where the polymer phase resulted in much more homogeneous strain field.

CRediT authorship contribution statement

Nicolò Arcieri: Methodology, Investigation, Validation, Data curation, Formal analysis, Writing – original draft. **Bin Chen:** Investigation, Data curation, Formal analysis. **Lars A. Berglund:** Conceptualization, Funding acquisition, Data curation, Writing – review & editing, Supervision. **Marcus Vinícius Tavares da Costa:** Conceptualization, Methodology, Investigation, Data curation, Writing – review & editing, Supervision.

Declaration of Competing Interest

The authors declare that they have no known competing financial interests or personal relationships that could have appeared to influence the work reported in this paper.

Data availability

Data will be made available on request.

Acknowledgements

The research funding within the KAW biocomposites program from Knut and Alice Wallenberg foundation through the Wallenberg Wood Science Center (WWSC) is acknowledged. Dr. Hui Chen is acknowledged for his support during the sample preparation. The authors thank Dr. Erik Jungstedt for the laser cutting assistance and discussion on the mechanics of wood-based materials. Prof. Federico Carosio is also acknowledged for fruitful discussion on the material science perspective.

Appendix A

Finite element calculation of J-integral for TW laminates

In the experimental procedure, wood was assumed to be isotropic. Here, fracture energy was estimated using the finite element method to compare with the previous procedure and experimental findings. In the FE-model, the material is orthotropic and critical force from experiments is used as a crack growth criterion. This section provides brief information on how to perform the calculation of the well-established path-independent J-integral before crack growth by evaluating the stress field from element gaussian points around the crack tip from the simulation that ultimately allows Eq. (8) to be computed. The model was implemented in the 2D plane strain module of the solid mechanics module in COMSOL Multiphysics where a half laminate beam is shown in Fig. A1. The thickness of each material has been taken from microscopy images — 0.5 μm for TW and 0.2 μm for PMMA layers — and all dimensions are from the experimental setup mentioned in the main body of this work. Displacements in the rollers was prescribed as in the experiments while a frictionless penalty contact between the beam and rollers were set. Symmetry boundary conditions were set on edges below the crack tip on the left of the beam. Higher-order quadrilateral elements were used with mesh refinements near the contours of element size of 0.02 mm.

For PMMA layers, the material model is isotropic linear elastic with Young's modulus of 2.4 GPa and the Poisson ratio of 0.35. For the TW laminates, it is orthotropic linear elastic since the moduli in tangential E_T and radial directions E_R are different, with elastic moduli of $E_T = 3.3$ GPa and $E_R = 4$ GPa and the Poisson ratio of $\nu_{TR} = 0.36$ estimated from Ref. [14]. The shear modulus was chosen to be $G_{TR} = 0.1$ GPa as the lowest value which provides a relatively good fit to the force–displacement data from all experiments shown in Fig. A.2a. Given the complex microstructure of TW layers, the simulation agreed well with all experiments in this work.

Fig. A.2b shows the computed values of J-integral from the three contours as a function of the prescribed displacement. No significant difference was found in the calculations. We then used the 1-mm contour in the manuscript, which account for the PMMA layers giving homogenized values for comparison to the experimental results. In addition, the stress fields from the simulations (at the displacement of 0.3 mm) are shown in Fig. A.2c depicting the complexity of the stress distribution near the crack tip. Minor contributions from the normal stress σ_R and shear stress σ_{TR}, which is expected from a four-point-bending setup.

Appendix B. Supplementary materials

Supplementary data to this article can be found online at https://doi.org/10.1016/j.compositesa.2023.107693.

References

[1] Gibson LJ, Ashby MF. Wood. Cellular Solids. Cambridge University Press; 1997. p. 387–428. https://doi.org/10.1017/CBO9781139878326.
[2] Ashby MF. Introduction. Materials and the Environment. Elsevier 2021:1–19. https://doi.org/10.1016/B978-0-12-821521-0.00001-3.
[3] Fu Q, Yan M, Jungstedt E, Yang X, Li Y, Berglund LA. Transparent plywood as a load-bearing and luminescent biocomposite. Compos Sci Technol 2018;164: 296–303. https://doi.org/10.1016/j.compscitech.2018.06.001.
[4] Ansell MP. Hybrid wood composites – integration of wood with other engineering materials. Wood Composites. Elsevier 2015:411–26. https://doi.org/10.1016/B978-1-78242-454-3.00016-0.
[5] Hill CAS. Wood Modification: Chemical, Thermal and Other Processes (Wiley Series in Renewable Resource). 1st ed. John Wiley & Sons; 2006.
[6] Montanari C, Ogawa Y, Olsén P, Berglund LA. High performance, fully bio-based, and optically transparent wood biocomposites. Adv Sci 2021;8. https://doi.org/10.1002/advs.202100559.
[7] Zhu M, Song J, Li T, Gong A, Wang Y, Dai J, et al. Highly anisotropic, highly transparent wood composites. Adv Mater 2016;28. https://doi.org/10.1002/adma.201600427.
[8] Montanari C, Olsén P, Berglund LA. Sustainable wood nanotechnologies for wood composites processed by in-situ polymerization. Front Chem 2021;9. https://doi.org/10.3389/fchem.2021.682883.
[9] Li Y, Fu Q, Yang X, Berglund L. Transparent wood for functional and structural applications. Philos Trans R Soc A Math Phys Eng Sci 2018;376:20170182. https://doi.org/10.1098/rsta.2017.0182.
[10] Li Y, Yang X, Fu Q, Rojas R, Yan M, Berglund L. Towards centimeter thick transparent wood through interface manipulation. J Mater Chem A Mater 2018;6: 1094–101. https://doi.org/10.1039/C7TA09973H.
[11] Qin J, Li X, Shao Y, Shi K, Zhao X, Feng T, et al. Optimization of delignification process for efficient preparation of transparent wood with high strength and high transmittance. Vacuum 2018;158:158–65. https://doi.org/10.1016/j.vacuum.2018.09.058.
[12] Lian M, Huang Y, Liu Y, Jiang D, Wu Z, Li B, et al. An overview of regenerable wood-based composites: preparation and applications for flame retardancy, enhanced mechanical properties, biomimicry, and transparency energy saving. Adv Compos Hybrid Mater 2022;5:1612–57. https://doi.org/10.1007/s42114-022-00475-6.
[13] Jungstedt E. Deformation and fracture behavior of transparent wood-polymer biocomposites. KTH Royal Institute of Technology 2022. PhD thesis.
[14] Jungstedt E, Montanari C, Östlund S, Berglund L. Mechanical properties of transparent high strength biocomposites from delignified wood veneer. Compos Part A Appl Sci Manuf 2020;133. https://doi.org/10.1016/j.compositesa.2020.105853.
[15] Koivurova M, Vasileva E, Li Y, Berglund L, Popov S. Complete spatial coherence characterization of quasi-random laser emission from dye doped transparent wood. Opt Express 2018;26:13474. https://doi.org/10.1364/OE.26.013474.
[16] Li Y, Yu S, Veinot JGC, Linnros J, Berglund L, Sychugov I. Luminescent transparent wood. Adv Opt Mater 2017;5:1600834. https://doi.org/10.1002/adom.201600834.
[17] Vasileva E, Li Y, Sychugov I, Mensi M, Berglund L, Popov S. Lasing from organic dye molecules embedded in transparent wood. Adv Opt Mater 2017;5:1700057. https://doi.org/10.1002/adom.201700057.
[18] Gan W, Gao L, Xiao S, Zhang W, Zhan X, Li J. Transparent magnetic wood composites based on immobilizing Fe3O4 nanoparticles into a delignified wood template. J Mater Sci 2017;52:3321–9. https://doi.org/10.1007/s10853-016-0619-8.
[19] Li Y, Cheng M, Jungstedt E, Xu B, Sun L, Berglund L. Optically transparent wood substrate for perovskite solar cells. ACS Sustain Chem Eng 2019;7:6061–7. https://doi.org/10.1021/acssuschemeng.8b06248.
[20] Li Y, Fu Q, Rojas R, Yan M, Lawoko M, Berglund L. Lignin-retaining transparent wood. ChemSusChem 2017;10:3445–51. https://doi.org/10.1002/cssc.201701089.
[21] Chen Q, Jiang Z, Pei X, Liu Y, Du R, Zhao G. Bio-inspired, epoxy-based lamellar composites with superior fracture toughness by delignified wood scaffold. Compos Sci Technol 2021;207:108739. https://doi.org/10.1016/j.compscitech.2021.108739.
[22] Jungstedt E, Östlund S, Berglund LA. Transverse fracture toughness of transparent wood biocomposites by FEM updating with cohesive zone fracture modeling. Compos Sci Technol 2022;225:109492. https://doi.org/10.1016/j.compscitech.2022.109492.
[23] Romanowicz M. Numerical assessment of the apparent fracture process zone length in wood under mode I condition using cohesive elements. Theor Appl Fract Mech 2022;118:103229. https://doi.org/10.1016/j.tafmec.2021.103229.
[24] Yu Y, Xin R, Zeng W, Liu W. Fracture resistance curves of wood in the longitudinal direction using digital image correlation technique. Theor Appl Fract Mech 2021; 114:102997. https://doi.org/10.1016/j.tafmec.2021.102997.
[25] Stanzl-Tschegg SE, Tan DM, Tschegg EK. New splitting method for wood fracture characterization. Wood Sci Technol 1995;29. https://doi.org/10.1007/BF00196930.
[26] Thelandersson S, Larsen HJ. Timber engineering. Chichester: John Wiley & Sons; 2003.
[27] Karl'a V. Update on research on transparent wood. IOP Conf Ser Mater Sci Eng 2019;566:012015. https://doi.org/10.1088/1757-899X/566/1/012015.
[28] Li Y, Fu Q, Yu S, Yan M, Berglund L. Optically transparent wood from a nanoporous cellulosic template: combining functional and structural performance. Biomacromolecules 2016;17:1358–64. https://doi.org/10.1021/acs.biomac.6b00145.
[29] Gere JM. Mechanics of materials. 5. ed. Pacific Grove, Calif: Brooks/Cole; 2001.
[30] Hein PRG, Brancheriau L. Comparison between three-point and four-point flexural tests to determine wood strength of Eucalyptus specimens. Maderas Ciencia y Tecnología 2018. https://doi.org/10.4067/S0718-221X2018005003401.
[31] Rice JR, Paris PC, Merkle JG. Some further results of J-Integral analysis and estimates. Progress in Flaw Growth and Fracture Toughness Testing, 100 Barr Harbor Drive, PO Box C700. West Conshohocken, PA 19428–2959: ASTM International; 1973. p. 231–45. https://doi.org/10.1520/STP49643S.
[32] Standard test method for determination of reference temperature, To, for ferritic steels in the transition range 1, 2019. https://doi.org/10.1520/E1921-19.
[33] Tukiainen P. Mode I fracture behaviour of Norway spruce and silver birch in the radial-tangential and tangential-radial crack orientations. Aalto University; 2016. PhD thesis.
[34] Ashby MF, Easterling KE, Harrysson R, Maiti SK. Fracture and toughness of woods. Proc R Soc Lond A Math Phys Sci 1985;398:261–80. https://doi.org/10.1098/rspa.1985.0034.
[35] Rice JR. A path independent integral and the approximate analysis of strain concentration by notches and cracks. J Appl Mech 1968;35:379–86. https://doi.org/10.1115/1.3601206.
[36] Gonzáles GLG, González JAO, Castro JTP, Freire JLF. A J-integral approach using digital image correlation for evaluating stress intensity factors in fatigue cracks with closure effects. Theor Appl Fract Mech 2017;90:14–21. https://doi.org/10.1016/j.tafmec.2017.02.008.
[37] Davenport JCW, Smith DJ. A study of superimposed fracture modes I, II and III on PMMA. Fatigue Fract Eng Mater Struct 1993;16:1125–33. https://doi.org/10.1111/j.1460-2695.1993.tb00082.x.
[38] Chen B, Jungstedt E. Fast and large-converge-radius inverse compositional Levenberg–Marquardt algorithm for digital image correlation: principle, validation, and open-source toolbox. Opt Lasers Eng 2022;151:106930. https://doi.org/10.1016/j.optlaseng.2021.106930.
[39] Schreier H, Orteu J-J, Sutton MA. Image Correlation for Shape, Motion and Deformation Measurements. Boston, MA: Springer, US; 2009. https://doi.org/10.1007/978-0-387-78747-3.
[40] Ostapska K, Malo KA. Calibration of a combined XFEM and mode I cohesive zone model based on DIC measurements of cracks in structural scale wood composites. Compos Sci Technol 2021;201:108503. https://doi.org/10.1016/j.compscitech.2020.108503.
[41] Krala G, Ubowska A, Kowalczyk K. Mechanical and thermal analysis of injection molded poly(methyl methacrylate) modified with 9,10-dihydro-9-oxa-10-phosphaphenanthrene-10-oxide (DOPO) fire retarder. Polym Eng Sci 2014;54:1030–7. https://doi.org/10.1002/pen.23644.